Effects of Zr substitution on structural, morphological, and magnetic properties of bismuth iron oxide phases

A Asif[1], M Hassan[1,†], S Riaz[2], S Naseem[2], and S S Hussain[2]

[1] *Materials Growth and Simulation Laboratory, Department of Physics, University of the Punjab, Lahore-54590, Pakistan*
[2] *Center of Excellence in Solid State Physics, University of the Punjab, Lahore-54590, Pakistan*

(Received 23 December 2016; revised manuscript received 1 May 2017; published online 10 July 2017)

The present study involves co-precipitation method to grow un-doped and Zr-doped bismuth iron oxide with $x_{Zr} =$ 0.10–0.30. The molar solutions of ferric chloride ($FeCl_3$), zirconyle chloride ($ZrOCl_2$), and bismuth chloride ($BiCl_3$) are prepared in distilled water, and are allowed to react with sodium hydroxide (NaOH). The synthesized powders are then converted into pellets, which are sintered at 500 °C for two hours in a muffle furnace. X-ray diffraction (XRD) shows multi-phase formation in un-doped and Zr doped samples. Scanning electron microscope (SEM) depicts layered structure at low Zr concentration $x_{Zr} = 0.10$, while uniform surface with smaller grains and voids is observed at $x_{Zr} = 0.20$, but at $x_{Zr} = 0.30$, cracks and voids become prominent. The ferromagnetic nature of the un-doped sample is observed by vibrating sample magnetometer (VSM), while paramagnetic behavior appears due to Zr doping. The ferromagnetism in un-doped sample is lost by Zr doping, which is due to the formation of additional Fe–O–Zr bonds that induce paramagnetic behavior.

Keywords: co-precipitation, multi-phases, ferromagnetism, paramagnetism, $BiFeO_3$

PACS: 75.50.Pp, 68.37.Hk, 61.05.cp, 81.10.Dn **DOI:** 10.1088/1674-1056/26/8/087502

1. Introduction

The search for promising and novel materials has forced the scientific community to find the critical parameters by conducting experiments[1–16] and using theoretical methodologies.[17–22] Therefore, it is needed to find the materials simultaneously exhibiting many ferroic characters such as ferromagnetism, ferroelectricity, and ferroelasticity, etc., which are termed as multiferroics.[23] These materials have applications in spintronic, sensors, data storage and the ferromagnetic resonance devices, which have electrically tunable characteristics.[24] Bismuth ferrite ($BiFeO_3$) is an important multiferroic material which was discovered in the late 1950s.[25] Its crystal structure is rhombohedrally distorted perovskite, which exhibits ferroelectricity below $T_C \sim 1100$ K and shows G-type antiferromagnetism up to $T_N \sim 650$ K.[26] The true ferroelectric nature of BFO has been confirmed by measuring ferroelectricity at 77 K,[27] which showed a remnant polarization $\sim 6.1\ \mu C \cdot cm^{-2}$ along [111]. A rhombohedral structure with space group $R3c$ has been found by using the single crystal x-ray diffractions (XRD) and the neutron diffraction investigations.[28] In the past ten years, over three thousand reports on bismuth ferrites have been published, which depict the material significance.[29] $BiFeO_3$ is probably the most prominent in all the known multiferroics because both its ferroelectric and antiferromagnetic orders are retained at the higher temperatures; therefore, it is highly suitable for room temperature applications.

In $BiFeO_3$, ferroelectricity is due to $6s^2$ lone pair electrons at the Bi ion,[30] while partially filled d-orbitals of Fe produce magnetism.[31] There are many drawbacks, which hinder its technological applications.[32] Single phase BFO is relatively difficult to achieve, because it remains stable in a narrow temperature range.[33] Secondary phases have been reported in many experimental studies. The weak magnetization at room temperature originates from its spatially modulated spin structure, and the various impurity phases cause high leakage current, which imposes restrictions to achieve intrinsic ferroelectricity.[32] The presence of the secondary phases results in valency fluctuations of iron between Fe^{+3} and Fe^{+2}, however, the presence of oxygen vacancies causes high leakage current problem.[34] By making the chemical substitutions during fabrication or by alloying with other perovskites, the properties of BFO have been reported to be improved.[35] It is found that substituting rare earth ions, such as La and Nd, leakage current decreases in BFO. By controlling the volatile nature of Bi atoms and suppressing the generation of oxygen vacancies, the charge compensation control is realized.[36] In this work, we add Zr^{+4} for substituting the B-site Fe, to study the effects on the structural, morphological and the magnetic properties of BFO. The Zr dopant is very less explored for $BiFeO_3$ and is selected to tune the physical properties of the host lattice to elucidate the potential multiferroic device applications. BFO nano-powders can be prepared by using different fabrication methods to obtain highest phase purity at the low fabrication temperatures to realize cost-effective samples.[24]

In this work, we use co-precipitation method, which is simple and cheap technique to prepare samples in the bulk form. The main advantage of this method is that it requires

†Corresponding author. E-mail: mahmood.physics@pu.edu.pk

© 2017 Chinese Physical Society and IOP Publishing Ltd

low synthesizing temperature. The effects of Zr substitution on the structural, morphological and the magnetic properties of the host lattice are systematically studied.

2. Experiment

Powders of un-doped and Zr-doped bismuth iron oxide are synthesized by co-precipitation method. The 0.5-molar solutions are prepared for growing the un-doped and Zr doped ($x_{Zr} = 0.10$, 0.20, and 0.30) bismuth iron oxide by using $BiCl_3$, $FeCl_3$, $ZrOCl_2 \cdot 8H_2O$, NaOH precursors, and mixing them in 50-ml distilled water. We have used sodium hydroxide (NaOH) as a precipitating agent. The prepared solution is stirred on a hot plate with a magnetic stirring for 30 min at 75 °C. The precipitates are separated from the solution by filtration using Whatman filter paper, and the precipitates are washed with distilled water. The filtrates are then dried at 45 °C in a drying oven for 6 h. The dried chunks are grinded to obtain uniform powders, which are calcined at 450 °C in a muffle furnace for 2 h. Then the powders are shaped into pellets by using hydraulic press under a pressure of 5 tons for 5 min. Afterwards, the pellets are further sintered at 500 °C in a muffle furnace for 2 h. The crystal structure of the samples is explored by using Bruker D8 advance x-ray diffractometer working at 40 kV and 40 mA and Cu Kα (1.5406 Å) radiation. The surface structure is observed by using Hitachi scanning electron microscopy (SEM). The Lakeshore's 7407 vibrating sample magnetometer is used with an applied magnetic field range of ±1 T, to elucidate the magnetic behavior of the fabricated samples.

3. Results and discussion

3.1. Structural properties

The XRD patterns of un-doped and Zr-doped BFO ($BiFe_{1-x}Zr_xO_3$) with $x = 0.10$, 0.20, and 0.30 are shown in Fig. 1. By matching with the JCPDS cards (01-071-2494, 00-025-0090, and 075391), we observed three phases belonging to rhombohedral $BiFeO_3$ with space group $R3c$, orthorhombic $Bi_2Fe_4O_9$ with space group $Pbam$, and cubic $Bi_{24}(Bi_{1.04}Fe_{0.84})O_{40}$ with space group $I23$, in both un-doped and Zr-doped samples. As can be observed in the XRD pattern of the un-doped sample, a multiphase formation occurs because the diffraction peaks from the crystallographic planes (110), (202), (300), (125), (220), (217), and (134) belonging to $BiFeO_3$ phase, while, the crystallographic planes (120), (002), (221), (221), (140), (141), (142), and (431) belong to $Bi_2Fe_4O_9$ phase. Similarly, (310), (222), (332), and (422) belong to $Bi_{24}(Bi_{1.04}Fe_{0.84})O_{40}$. The XRD patterns show that the (120) plane belonging to $Bi_2Fe_4O_9$ phase has the highest intensity among all the diffraction peaks in the un-doped sample. With Zr doping at $x_{Zr} = 0.10$, the highest peak shifts to (141) plane, which also belongs to $Bi_2Fe_4O_9$ phase. By increasing Zr doping $x_{Zr} = 0.20$–0.30, the highest peak again belongs to (120) plane of $Bi_2Fe_4O_9$. Due to equivalent thermal stabilities of all the appeared BFO phases, it is difficult to predict which phase makes dominant contributions to the stability. However, under the present employed growth and post-growth conditions, $Bi_2Fe_4O_9$ appears as a dominant phase. Remaining peaks belong to $BiFeO_3$ and $Bi_{24}(Bi_{1.04}Fe_{0.84})O_{40}$ phases. The XRD results confirm that Zr-doped samples have the crystallographic phases, which are similar to those observed in the undoped sample. It means that crystalline structure of undoped sample is not affected by Zr substitution, because ZrO_2 peaks appear in none of all the XRD patterns of Zr-doped samples, which depicts the substitutional replacement of Zr dopants with the host lattice cations. The multi-phase formation during the growth of $BiFeO_3$ is a common issue, which has already been reported in many previous experiments.[37–41] It is also interesting to note that all the compounds formed have Bi, Fe and O as constituents and peaks belonging to none of their binaries (Bi_2O_3, Fe_2O_3, etc.) are present. Therefore, it is evident that under the employed growth conditions, in addition to the $BiFeO_3$ (BFO) phase formation, various ternary peaks belonging to various BFO phases also appear, which is due to having a narrow equivalent temperature range in which they have equivalent thermal stabilities. The observed fact of the appearance of multi-phase formation is in accordance with the earlier reports,[38,42] however, several reports on the single phase formation of $BiFeO_3$ are also present in the literature.[43,44] Therefore, single phase BFO could be realized by employing a set of optimized fabrication conditions. The formation of multi-phases is due to the fact that in addition to $BiFeO_3$ there is more than one thermodynamically stable possible phases[42] that arises under the employed growth conditions. Therefore, the absence of ZrO_2 peaks reveals Zr substitutions with Fe cations of the formed multi-phase.

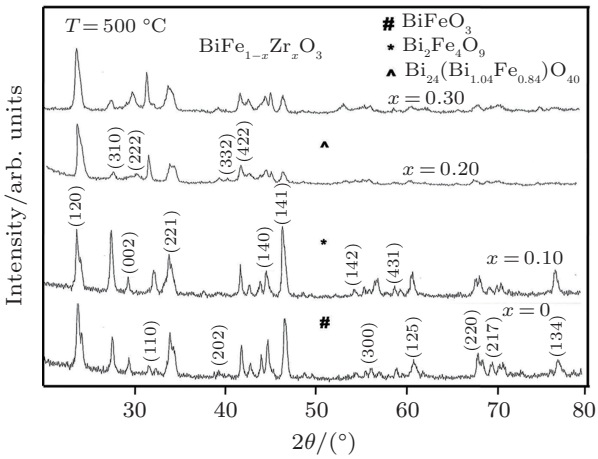


Fig. 1. XRD patterns of bismuth manganese oxide with $x_{Zr} = 0.00$, 0.10, 0.20, and 0.30, grown by co-precipitation method.

The average crystallite size of sample is calculated by using the Scherrer formula from the major diffraction peaks of each phase

$$t = \frac{0.9\lambda}{\beta \cos(\theta)}, \tag{1}$$

where, t, λ, β, and θ represent crystallite size, impinging x-rays wavelength, full-width at half-maximum (FWHM), and the diffraction angle, respectively. The crystallite sizes of all three phases are shown in Fig. 2. The crystallite size of $BiFeO_3$ phase is smaller at $x_{Zr} = 0.00$ and $x_{Zr} = 0.10$, but increases due to Zr substitution at $x_{Zr} = 0.20$–0.30. The crystallite size of $Bi_2Fe_4O_9$ is higher at $x_{Zr} = 0.00$, however, it slightly decreases at $x_{Zr} = 0.10$–0.30. The third phase $Bi_{24}(Bi_{1.04}Fe_{0.84})O_{40}$ has almost constant crystallite size by substituting Zr except at $x_{Zr} = 0.30$, where it decreases below 175nm, which might be due to the crystallite size of $BiFeO_3$ increasing to more than 275 nm.

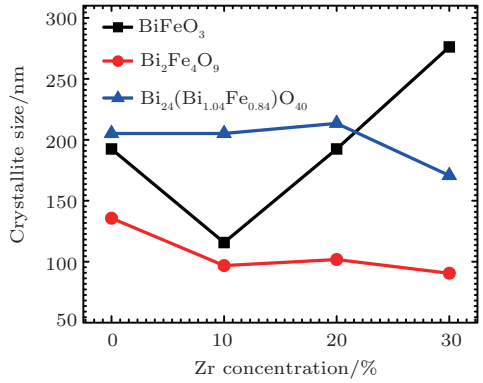


Fig. 2. (color online) Plots of crystallite size of $BiFeO_3$, $Bi_2Fe_4O_9$ and $Bi_{24}(Bi_{1.04}Fe_{0.84})O_{40}$ versus Zr doping content.

The behaviors of relative intensity of $BiFeO_3$, $Bi_2Fe_4O_9$, and $Bi_{24}(Bi_{1.04}Fe_{0.84})O_{40}$ phases with respect to Zr substitution are shown in Fig. 3. The relative intensity of $BiFeO_3$ increases with increasing Zr, while for $Bi_{24}(Bi_{1.04}Fe_{0.84})O_{40}$ its relative intensity decreases. The relative intensity of $Bi_2Fe_4O_9$ remains almost constant. Therefore, at higher Zr doping, the $BiFeO_3$ phase formation enhances, however, $Bi_2Fe_4O_9$ remains as a major phase.

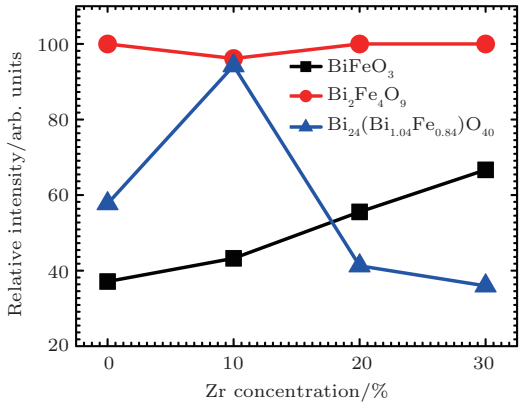


Fig. 3. (color online) Plots of relative intensity of $BiFeO_3$, $Bi_2Fe_4O_9$, and $Bi_{24}(Bi_{1.04}Fe_{0.84})O_{40}$ versus Zr substituting concentration for $x_{Zr} = 0.00$, 0.10, 0.20, and 0.30.

3.2. Surface morphology

The surface morphologies of undoped and doped samples are measured by using scanning electron microscopy (SEM). The SEM micrographs of un-doped BFO and doped samples are shown in Fig. 4. The un-doped and Zr-doped (with $x_{Zr} = 0.10$) samples reveal that the surface consists of stacked layers. By increasing doping concentration of Zr to $x_{Zr} = 0.20$, uniform surfaces having small grains, along with some voids, are observed. The higher doping of Zr ($x_{Zr} = 0.20$) leads to the formation of grains but voids and cracks still appear on the surface. Wang and Nan[26] reported that the grain size decreases due to Zr doping and various pores appears on the surface of the $BiFeO_3$ film.

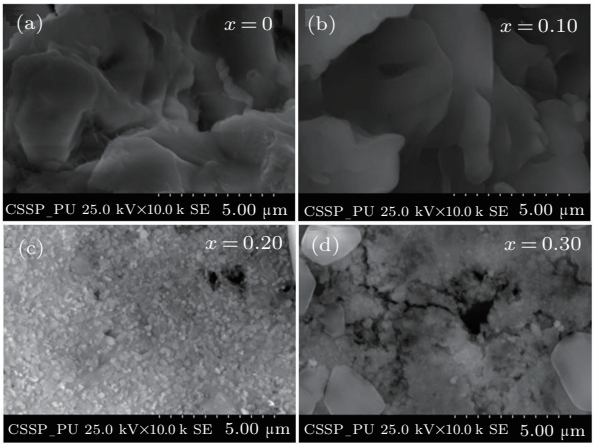


Fig. 4. SEM micrographs of bismuth iron oxide with (a) $x_{Zr} = 0.00$, (b) $x_{Zr} = 0.10$, (c) $x_{Zr} = 0.20$, and (d) $x_{Zr} = 0.30$.

The variation in the surface morphology seems to be closely related to the variation of relative intensity as depicted in Fig. 3, where it can be observed that relative intensity of $Bi_2Fe_4O_9$ remains constant, therefore, its effect on the surface morphology can be ignored. However, the remaining two phases have their relative intensities increasing up to $x_{Zr} = 0.10$ and the surface morphologies of both samples show similar layered structures. While, the surface morphology significantly changes at $x_{Zr} = 0.20$, indicating that the small grains might be related to $BiFeO_3$ phase because its relative intensity continuously increases with Zr. The surface pores can be approximately related to the appreciable decreasing of relative intensity of $Bi_{24}(Bi_{1.04}Fe_{0.84})O_{40}$ phase as depicted in Fig. 3. The comparison of the grain morphology with the XRD peak intensity is very important to study the material behaviors under different growth conditions, and has been already explored in various experimental reports.[45–47]

The surface morphology for the sample with $x_{Zr} = 0.30$ as shown by SEM image in Fig. 4, also supports the fact observed above. The surface has bigger uniform grains, and these grains may arise from the smaller agglomerated grains, which is again shown to be related to $BiFeO_3$, because XRD

relative intensity still increases, as depicted in Fig. 3. This evidences the continuous growth of $BiFeO_3$. While, the pores and cracks at the surface may be attributed to the decrease of relative intensity of $Bi_{24}(Bi_{1.04}Fe_{0.84})O_{40}$. Moreover, the increase in relative intensity of the $BiFeO_3$ phase, which may be considered to determine the surface morphology, is also supported by calculated the crystallite size as shown in Fig. 2, where the crystallite size of $BiFeO_3$ also increases with x_{Zr}. Therefore, smaller and larger uniform grains at the surfaces of the samples with $x_{Zr} = 0.20$ and $x_{Zr} = 0.30$, respectively, belongs to $BiFeO_3$ phase.

As indicated by XRD study, no ZrO_2 phase belonging to impurity element is observed and only multi-phases of $BiFeO_3$, $Bi_2Fe_4O_9$, and $Bi_{24}(Bi_{1.04}Fe_{0.84})O_{40}$ are present. The surface morphology does not indicate the presence of ZrO_2 like impurity phases (as no wide differences in the contrast of SEM images are present). Therefore, from both XRD and SEM study, we can observe that Zr has been substituted for Fe, despite of the multi-phase formation. Although, multi-phase appearance has been observed by XRD, the absence of wide differences in contrast evidences that the SEM morphology, as observed in the present case, cannot be employed to differentiate various phases.

3.3. Magnetic properties

Magnetic behaviors of the synthesized samples are measured by vibrating sample magnetometer (VSM) at room temperature. The measured magnetization curves are shown in Fig. 5, in which the inset shows the magnified part of the graph in the applied magnetic field range ±1500 Oe (1 Oe = 79.5775 A/m). The hysteresis loop with small saturation magnetization is observed for the un-doped sample, while all Zr-doped samples show paramagnetic behaviors. Weak ferromagnetism is already observed in un-doped sample, which is different from that in the bulk BFO.[48] There may be several reasons for the observed weak ferromagnetism. Since iron has fluctuating valency between $Fe^{+3}$and Fe^{+2}, the possible double exchange interaction between Fe^{+2} and Fe^{+3} through the oxygen can produce ferromagnetism. Magnetization may also be produced due to structural distortion in BFO. The size effect and canting of antiferromagnetic spin order structure might produce weak ferromagnetism. It is already observed that the magnetization increases in BFO by reducing the particle size, because spiral spin ordering is partially suppressed due to the finite size effect of the prepared nanoparticles.[49] Ferromagnetic behavior is completely lost due to the substitution of Zr for Fe. The substitution of Zr^{+4} ions at the Fe-sites produces lattice distortion, which results in the modifications of the existing Fe–O–Fe bond lengths and the bond angles. Zr^{+4} being magnetically inactive does not directly contribute to the magnetization. Subsequently, replacement of magnetically inactive Zr^{+4} ion may result in the dominated non-magnetic tendency rather than the structural distortion, hence, ferromagnetism is avoided. The super-exchange interaction between the antiferromagnetically aligned Fe^{+3} ions is controlled by Fe–O–Fe bond angles through the oxygen anions.[50] The formation of additional Fe–O–Zr bonds, due to increasing Zr doping, are responsible for reducing the magnetization. Since multi-phases of un-doped and Zr-doped samples are shown by XRD, the addition of Zr further disturbs the crystal structure, hence the ferromagnetism is completely lost. The addition of Zr reduces the strength of Fe^{+3}–O–Fe^{+2} interaction, which is responsible for mediating the ferromagnetism. The deterioration in ferromagnetism is due to the multi-phase formation and the applied sintering temperatures, which weaken the ferromagnetic interactions. Of course, the vanishing of ferromagnetism is not suitable for the useful device applications; however, the employed growth conditions can be tuned in future to prepare Zr-doped single phase $BiFeO_3$ exhibiting appreciable magnetization.

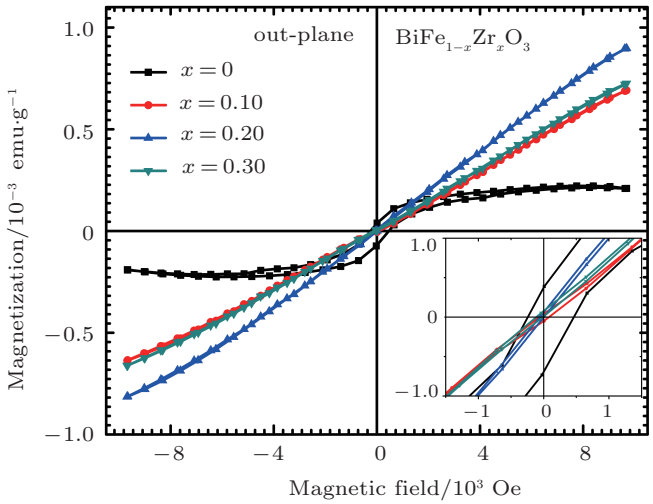


Fig. 5. (color online) Magnetization curves for bismuth iron oxide with $x_{Zr} = 0.00$, 0.10, 0.20, and 0.30, measured by vibrating sample magnetometer (VSM) at room temperature with ±1 T of the applied magnetic field.

Figure 6 shows the magnetization at 1 T, indicating that the net magnitude of paramagnetic signal increases with Zr except at $x_{Zr} = 0.30$, which may be due to the surface imperfection as depicted in Fig. 4. The magnetic properties elucidated by VSM are also more closely related to the surface morphology (Fig. 4) as determined by SEM, and crystallite size and relative intensity (Figs. 2 and 3) calculated from the measured XRD patterns. As shown in Fig. 6, the magnetization continuously increases up to $x_{Zr} = 0.20$, above which, it slightly decreases. The sample without Zr has ferromagnetism, which disappears upon Zr addition. This approximately linear increase in M (at 1 T) is related to the $BiFeO_3$ phase, whose

crystallite size (see Fig. 2) and relative intensity (see Fig. 3) increase with increasing Zr up to $x_{Zr} = 0.20$. A similar evidence about the growth of $BiFeO_3$ is also demonstrated by SEM images. However, decrease in magnetization M (at 1 T) at $x_{Zr} = 0.30$, can be justified due to the imperfection (cracks, pores) as evidenced in SEM image in Fig. 4, which may induce the residual stresses to reduce M at 1 T. The magnetic characteristics of the grown samples are closely related to the surface characteristic and the crystal structure, therefore, under the employed growth conditions, the information about the formed phases may be useful in understanding the material characteristics for the applications in practical devices.

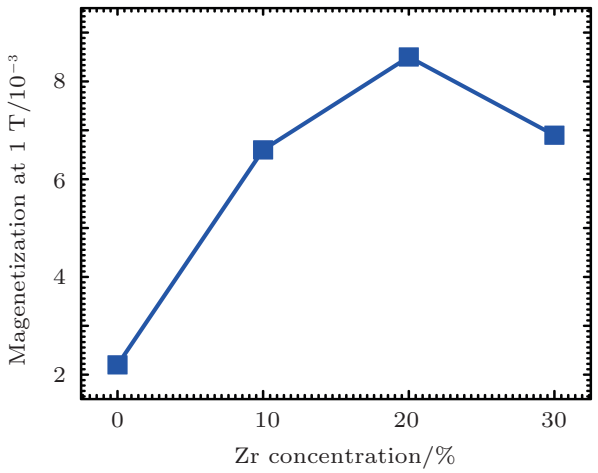


Fig. 6. (color online) Variation in magnetization at 10^4 Oe with Zr doping, extracted from magnetization curves as given in Fig. 5.

4. Conclusions

Un-doped and Zr-doped bismuth iron–oxide samples are synthesized by the co-precipitation method. The XRD patterns illustrate the appearance of three phases $BiFeO_3$, $Bi_2Fe_4O_9$, and $Bi_{24}(Bi_{1.04}Fe_{0.84})O_{40}$. The similar structural phases appear before and after adding Zr into the host lattice, which indicates the perfect Zr-substitution for the cations of the existing crystalline multi-phases of bismuth iron oxide. The $Bi_2Fe_4O_9$ appears as a dominant phase in all the grown samples, while the relative intensity and crystallite size of $BiFeO_3$ increase with Zr, indicating that $BiFeO_3$ phase formation is most preferential. The SEM micrographs of the un-doped and the sample doped with $x_{Zr} = 0.10$, show the layered structure. The uniformity of the surface is enhanced with further increasing Zr content, however, some cracks and voids also appear. Magnetization curves measured by VSM at room temperature (RT) show that the weak ferromagnetism is exhibited by un-doped sample, while paramagnetic behavior is present in Zr-doped sample. The Zr doping is observed to degrade the ferromagnetism, as the Zr-substitution in multi-phases modifies the existing crystal structure, resulting in completely lost ferromagnetism. Therefore, Zr substitution within the formed multi-phases of bismuth iron oxide provides new information about the phase stability and corresponding surface and magnetic characteristics, which may be useful in realizing the single phase $BiFeO_3$ in future.

Acknowledgment

One of the authors (M Hassan) is thankful to University of the Punjab, Lahore, for financial support through faculty research grant program for the year 2017–2018.

References

[1] Lv Z, Zhang J, Niu W, Zhang M, Song L, Zhu H and Wang X 2016 *Chin. Phys. B* **25** 097502
[2] Parveen B, Hassan M Khalid Z, Riaz S and Naseem S 2017 *J. Appl. Res. Technol.* **15** 132
[3] Dong Z, Feng Z Y, Bai M X, Quan L S, Zhi H J, Gang Z M, Sheng W C and Bo Y J 2015 *Chin. Phys. Lett.* **32** 127502
[4] Hassan M, Irfan R, Riaz S, Naseem S, Hussain S S and Murtaza G 2017 *J. Korean Phys. Soc.* **70** 460
[5] Imran M M, Ying S, Hao D S, Wen S K, Wei H P and Cong W 2015 *Chin. Phys. Lett.* **32** 67503
[6] Yan L H, Hong L Z, Tian L G and Qiao M X 2016 *Acta Phys. Sin.* **65** 048102 (in Chinese)
[7] Yong Y, Ling X C, Liang Q, Hua L X and Shen L F 2010 *Chin. Phys. Lett.* **27** 057501
[8] Hassan M, Younas S, Sher F, Husain S S, Riaz S and Naseem S 2017 *Appl. Phys. A* **123** 352
[9] Hui H G, Wei L L and Umehara I 2016 *Chin. Phys. B* **25** 067501
[10] Jing G and Ling S L 2015 *Acta Phys. Sin.* **64** 217406 (in Chinese)
[11] Bao L F, Huang W D and Ren Y J 2016 *Chin. Phys. Lett.* **33** 77502
[12] Ling Z S, Ye C W and Yong Z 2015 *Acta Phys. Sin.* **64** 167501 (in Chinese)
[13] Cheng L Y, Ying Z, Lin G W, Gui Y Y and Zhong F 2007 *Physics* **36** 0
[14] Dong H X, Yi X Z, Rui W E, Liang C G and Ping L Z 2010 *Chin. Phys. Lett.* **27** 117502
[15] Hua C Y, Jing P R, Hao S Y, Ting L T, Min W Z, Dong L G and Ting C Y 2016 *Acta Phys. Sin.* **65** 087102 (in Chinese)
[16] Abid A, Hassan M, Hussain S S, Riaz S and Naseem S 2017 *J. Supercond. Nov. Magn.* doi:10.1007/s10948-017-4067-8
[17] Yu Y Z, Li S, Mei P M and Juan S S 2016 *Acta Phys. Sin.* **65** 127501 (in Chinese)
[18] Chun P F, Peng C Z, ling L X, Fu Z, Ming W X and Ming C H 2016 *Chin. Phys. B* **25** 096108
[19] Mahmood Q and Hassan M 2017 *J. Alloys Compd.* **704** 659
[20] Sattar M A, Rashid M, Hashmi M R, Ahmad S A, Imran M and Hussain F 2016 *Chin. Phys. B* **25** 107402
[21] Hassan M, Noor N A, Mahmood Q and Amin B 2016 *Curr. Appl. Phys.* **16** 1473
[22] Ying X H, Yu C, Chen J, Xiang J S, Yao Y M, Ying G Z, Kun L, Qi C M and Yi Z G 2016 *Chin. Phys. B* **25** 067503
[23] Murari N M, Thomas R, Melgarejo R E, Pavunny S P and Katiyar R S 2009 *J. Appl. Phys.* **106** 014103
[24] Shami M Y, Awan M S, Rehman M A U 2011 *J. Alloys Compd.* **509** 10139
[25] Martin L W, Chu Y H, Ramesh R 2010 *Mater. Sci. Eng. R* **68** 89
[26] Wang Y and Nan C W 2007 *Ferroelectrics* **357** 172
[27] Teague J R, Gerson R and James WJ 1963 *Solid State Commun.* **8** 1073
[28] Michel C, Moreau J M, Achenbach G D, Gerson R and James W 1969 *Solid State Commun.* **7** 701
[29] Rojac T, Bencan A, Malic B, Tutuncu G, Jones J L, Daniels J E and Damjanovic D 2014 *J. Am. Ceram. Soc.* **97** 1993
[30] Li C X, Yang B, Zhang S T, Liu D Q, Zhang R, Sun Y and Cao W W 2014 *J. Alloys Compd.* **590** 346
[31] Mao W W, Wang X F, Han Y M, Li X A, Li Y T, Wang Y F, Ma Y W, Feng X M, Yang T, Yang J P and Huang W 2014 *J. Alloys Compd.* **584** 520

[32] Li C X, Yang B, Zhang S T, Liu D Q, Zhang R, Sun Y and Cao W W 2014 *J. Alloys Compd.* **590** 346
[33] Nalwa K S and Garg A 2008 *J. Appl. Phys.* **103** 044101
[34] Jee S M, Gupta R, Garg A, Bansal V and Bhargava S 2010 *J. Appl. Phys.* **107** 123535
[35] Gheorghiua F P, Ianculescub A, Postolachea P, Lupuc N, Dobromira M, Lucaa D and Mitoseriua L 2010 *J. Alloys Compd.* **506** 862
[36] Singh S K and Ishiwara H 2006 *Jpn. J. Appl. Phys.* **45** 3194
[37] Kim J K, Kim S S and Kim W J 2005 *Mater. Lett.* **59** 4006
[38] Sharma S, Singh V, Kotnala R K, Dwivedi R K 2014 *J. Mater. Sci: Mater. Electron* **25** 1915
[39] Pradhan A K, Zhang K, Hunter D, Dadson J B and Loutts G B 2005 *J. Appl. Phys.* **97** 093903
[40] Riaz S, Shah S M H, Akbar A, Kayani Z N and Naseem S 2014 *IEEE Trans. Magn.* **50** 8
[41] Xie J, Feng C, Pan X and Liu Y 2014 *Ceram. Int.* **40** 703
[42] Muneeswaran M, Jegatheesan P and Giridharan N V 2013 *J. Exp. Nanosci.* **8** 341
[43] Naganuma H and Okamura S 2007 *J. Appl. Phys.* **101** 09M103.
[44] Layek S and Vera H C 2012 *Adv. Mat. Lett.* **3** 533
[45] Inoue M and Hirasawa I 2013 *J. Cryst. Growth* **380** 169
[46] Moret M, Chaaya A A, Bechelany M, Miele P, Robin Y and Briot O 2014 *Superlattices Microstruct.* **75** 477
[47] Song J M, Chen W T, Hsieh K H, Kao T H, Chen I G, Chiu S J and Lee H Y 2014 *Nano Res. Lett.* **9** 438
[48] Zhang S T, Lu M H, Wu D, Chen Y F and Ming N B 2005 *Appl. Phys. Lett.* **87** 262907
[49] Layek S and Vera H C 2012 *Adv. Mater. Lett.* **3** 533
[50] Arora M, Chauhan S, Sati P C, Kumar M, Chhoker S and Kotnala R K 2012 *J. Appl. Phys.* **112** 094102